Journal of Alloys and Compounds 725 (2017) 1098–1105

Contents lists available at ScienceDirect

Journal of Alloys and Compounds

journal homepage: http://www.elsevier.com/locate/jalcom

Ab-initio, magnetic, and ^{155}Gd Mössbauer spectroscopy study of $GdRhO_3$

Farshad Nejadsattari [a], Pu Wang [b], Zbigniew M. Stadnik [a, *], Yujiro Nagata [c], Tomohiro Ohnishi [c]

[a] Department of Physics, University of Ottawa, Ottawa, Ontario, K1N 6N5, Canada
[b] Key Laboratory of Extreme Conditions Physics, The Institute of Physics, Chinese Academy of Sciences, Beijing 100190, People's Republic of China
[c] College of Science and Engineering, Aoyama Gakuin University, Fuchinobe, Sagamihara, Kanagawa, 157-8572, Japan

ARTICLE INFO

Article history:
Received 27 April 2017
Received in revised form
19 June 2017
Accepted 23 July 2017
Available online 27 July 2017

Keywords:
Antiferromagnet
^{155}Gd Mössbauer spectroscopy
Electric quadrupole splitting
Electronic structure
Debye temperature

ABSTRACT

The results of X-ray diffraction, magnetic, and ^{155}Gd Mössbauer spectroscopy study, complemented by the *ab-initio* electronic structure and the hyperfine-interaction parameters calculations, of the $GdRhO_3$ orthorhodite are reported. $GdRhO_3$ crystallizes in the orthorhombic space group *Pnma* with the lattice parameters $a = 5.7450(1)$ Å, $b = 7.6647(1)$ Å, and $c = 5.2905(1)$ Å. The evidence is provided for the presence of directional covalent bonding between the Rh and O atoms and of ionic bonding between the Gd and Rh/O atoms. $GdRhO_3$ orders antiferromagnetically with the Néel temperature $T_N = 2.13(5)$ K. The magnetic susceptibility above T_N follows the modified Curie-Weiss law with the paramagnetic Curie temperature of $-3.37(1)$ K and the effective magnetic moment of 7.99(1) μ_B per Gd atom. The Debye temperature of $GdRhO_3$ determined from the Mössbauer data is found to be 256(1) K. The calculated Gd magnetic moment and hyperfine-interaction parameters are in good agreement with the experimental values.

1. Introduction

The compounds of the chemical formula ABO_3 are the perovskite-type oxides in which A is a large cation and B is a smaller cation. They are one of the most extensively studied oxide systems. Rare-earth (R) orthorhodites, $RRhO_3$, are a subset of these compounds [1] and their physical properties have been much less studied.

The $LuRhO_3$ orthorhodite was shown to be a *p*-type semiconductor that acts as a good hydrogen reduction catalyst [2]. This orthorhodite was found to be nonmagnetic down to 2.0 K, and its Debye temperature was determined to be 271 K [3]. The temperature dependence of the electrical resistivity of other $RRhO_3$ orthorhodites (R = La, Nd, Sm, Eu, Gd, Dy, Er, and Lu) [4] confirmed that they are semiconductors. The magnetic and specific heat measurements of the $RRhO_3$ orthorhodites (R = rare-earth except Ce and Pm) showed that they are either antiferromagnets or paramagnets [4,5].

The aim of this work is to explore structural, electronic, magnetic, and hyperfine-interaction properties of the $GdRhO_3$ orthorhodites. To this end, X-ray diffraction, magnetic, and ^{155}Gd Mössbauer spectroscopy measurements, complemented by the first-principles electronic structure and hyperfine-interaction parameters calculations, have been carried out and the results are presented and discussed here.

2. Experimental and theoretical methods

A polycrystalline sample of composition $GdRhO_3$ was synthesized by the solid-state reaction method using high-purity (99.9%) oxides of Rh_2O_3 and Gd_2O_3 [4]. An appropriate amount of oxides was thoroughly mixed and then pelletized under the pressure of 100 kg/cm^2. The pellet was calcined at 1223 K for 10 h in an oxygen atmosphere (1 atm). The mixing, pelletization, and calcination were repeated three times. Finally, after being reground and pressed into a pellet, the mixture was sintered at 1473 K for 12 h in an oxygen atmosphere (1 atm).

The X-ray diffraction (XRD) spectrum of $GdRhO_3$ was measured at 298 K in Bragg-Brentano geometry on a PANalytical X'Pert scanning diffractometer using Cu $K\alpha$ radiation in the 2θ range

* Corresponding author.
E-mail address: stadnik@uottawa.ca (Z.M. Stadnik).

http://dx.doi.org/10.1016/j.jallcom.2017.07.233
0925-8388/

15–85° in steps of 0.02°. The $K\beta$ line was eliminated by using a Kevex PSi2 Peltier-cooled solid-state Si detector.

The dc magnetic susceptibility was measured with a Quantum Design (QD) Magnetic Property Measurement System in the temperature range 1.8–300 K.

The ^{155}Gd Mössbauer measurements were done using a standard Mössbauer spectrometer operating in a sine mode and a source of ^{155}Eu($SmPd_3$). The source was kept at the same temperature as that of the absorber. The spectrometer was calibrated with a Michelson interferometer [6], and the spectra were folded. The Mössbauer absorber was made of pulverized material pressed into a pellet which was inserted into an Al disk container of the thickness of 0.008 mm to ensure a uniform temperature over the whole Mössbauer absorber. The surface density of the Mössbauer absorber of $GdRhO_3$ was 344 mg/cm^2. The 86.5 keV γ-rays were detected with a 2.5 cm NaI(Tl) scintillation detector covered with a 0.6 mm Pb plate to cut off the 105.3 keV γ-rays emitted from the source.

The analysis of the Mössbauer spectra involved a least-squares fitting procedure which entailed calculations of the positions and relative intensities of the absorption lines by numerical diagonalization of the full hyperfine interaction Hamiltonian. In the principal axis coordinate system of the electric field gradient (EFG) tensor, the Hamiltonian can be written as [7]

$$\widehat{H} = g\mu_B H_{hf}\left[\widehat{I}_z\cos\theta + \frac{1}{2}\left(\widehat{I}_+ e^{-i\phi} + \widehat{I}_- e^{i\phi}\right)\sin\theta\right] + \frac{eQV_{zz}}{4I(2I-1)}\left[3\widehat{I}_z^2 - I(I+1) + \frac{\eta}{2}\left(\widehat{I}_+^2 + \widehat{I}_-^2\right)\right], \quad (1)$$

where g is a nuclear g-factor of a nuclear state, μ_B is the nuclear Bohr magneton, H_{hf} is the hyperfine magnetic field at a nuclear site, Q is the quadrupole moment of a nuclear state, I is the nuclear spin, V_{zz} is the z component of the EFG tensor, η is the asymmetry parameter defined as $\eta = |(V_{xx} - V_{yy})/V_{zz}|$ (if the principal axes are chosen such that $|V_{xx}| < |V_{yy}| < |V_{zz}|$, then $0 \le \eta \le 1$), θ is the angle between the direction of H_{hf} and the V_{zz}-axis, ϕ is the angle between the V_{xx}-axis and the projection of H_{hf} onto the xy plane, and the $\widehat{I}_z$, $\widehat{I}_+$, and $\widehat{I}_-$ operators have their usual meaning. During the fitting procedure, the g factor and the quadrupole moment ratios for ^{155}Gd ($I_g = 3/2$, $I_{ex} = 5/2$) were constrained to $g_{ex}/g_g = 1.235$ and $Q_{ex}/Q_g = 0.087$, respectively [8]. The interference factor ξ for the E1 transition of 86.5-keV in ^{155}Gd was fixed to the value of 0.0520 which was derived from the fit of the ^{155}Gd Mössbauer spectrum of $GdFe_2$ at 4.2 K [9].

The surface density of the Mössbauer absorber corresponds to an effective thickness parameter [7] $T_a = 33.4 f_a$, where f_a is the Debye-Waller factor of the absorber. Since $T_a > 1$, the resonance line shape of the Mössbauer spectrum was described using a transmission integral formula [10]. In addition to the hyperfine parameters, only f_a and the absorber linewidth Γ_a were fitted as independent parameters. The source linewidth $\Gamma_s = 0.334$ mm/s and the background-corrected Debye-Waller factor of the source $f_s^* = 0.106$ [10], which were derived from the fit of the ^{155}Gd Mössbauer spectrum of $GdFe_2$ at 4.2 K [9], were used. The ^{155}Eu($SmPd_3$) source at 1.5 K emits a broadened emission line; it was found from the fit of the ^{155}Gd Mössbauer spectrum of GdFe2 at 1.5 K that $\Gamma_s = 0.708$ mm/s [9].

Ab initio electronic structure and Mössbauer hyperfine-interaction parameter calculations have been performed within the framework of density functional theory using the full-potential linearized augmented-plane-wave plus local orbitals (FP-LAPW+lo) method as implemented in the WIEN2k package [11]. In this method, one partitions the unit cell into two regions: a region of non-overlapping muffin-tin (MT) spheres centered at the atomic sites and an interstitial region. The wave functions in the MT regions are a linear combination of atomic radial functions times spherical harmonics, whereas in the interstitial regions they are expanded in plane waves. The basis set inside each MT sphere is split into a core and a valence subset. The core states are treated within the spherical part of the potential only and are assumed to have a spherically symmetric charge density in the MT spheres. The valence wave functions in the interstitial region were expanded in spherical harmonics up to $l = 4$, whereas in the MT region they were expanded to a maximum of $l = 12$ harmonics. For the exchange-correlation potential, the generalized gradient approximation (GGA) scheme of Perdew, Burke, and Ernzerhof [12] was used. The Hubbard parameter $U = 8.2$ eV and the exchange parameter $J = 0.68$ eV were used for the Gd 4f states [13]. A separation energy of −6.5 Ry between the valence and core states of individual atoms in the unit cell was chosen. The values of 2.14, 1.98, and 1.70 a.u. were used as the MT radii for Gd, Rh, and O, respectively. The plane-wave cut-off parameter was set to $R_{MT} \times K_{MAX} = 6.5$, where R_{MT} is the smallest MT radius in the unit cell and K_{MAX} is the maximum K vector used in the plane-wave expansion in the interstitial region. A total number of 120 inequivalent k-points was used within a $10 \times 8 \times 11$ k-mesh in the irreducible wedge of the first Brillouin zone. A convergence criterion for self-consistent field calculations was chosen in such a way that the difference in energy between two successive iterations did not exceed 10^{-4} Ry. The experimental lattice parameters (a, b, and c) and the atomic position parameters in the space group *Pnma* (*vide infra*) were used in the calculations.

3. Results and discussion

3.1. Structural characterization

The room-temperature X-ray powder diffraction pattern of $GdRhO_3$ is shown in Fig. 1. The studied compound crystallizes in the orthorhombic space group *Pnma* (No. 62) [1]. A Rietveld refinement [14] of the pattern in Fig. 1 yields the lattice parameters $a = 5.7450(1)$ Å, $b = 7.6647(1)$ Å, $c = 5.2905(1)$ Å, and the atomic positional parameters that are listed in Table 1.

The values of these parameters compare well with the corresponding values reported earlier [1]. The presence of no second phase/phases could be detected in the X-ray powder diffraction pattern of $GdRhO_3$ (Fig. 1).

The crystal structure of $GdRhO_3$ is shown in Fig. 2. One observes that the unit cell is a cuboid elongated along the b-direction. Thus, a larger separation between atoms along that direction causes relatively weak electrostatic interactions between them (*vide infra*). There are four formula units of $GdRhO_3$ per unit cell. The Gd and Rh atoms form chemical bonds with their O atom neighbors. These bonds are depicted in Fig. 2 by the connecting rods. They form an internal network between neighboring atoms and are responsible for the delocalization of the valence states (*vide infra*). The chemical bonds between Gd ions and the RhO_3 units are ionic, whereas the bonds between the Rh and O atoms in the RhO_3 units are covalent (*vide infra*). Based on the calculated electron charge density distributions and the calculated electronic structure, the nature of various bonds in $GdRhO_3$ is discussed below.

3.2. Ab-initio calculations

3.2.1. Charge density distributions

The nature of the interatomic interactions in $GdRhO_3$ is a

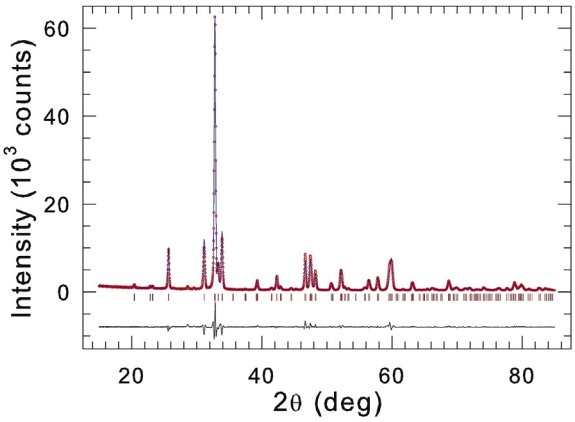

Fig. 1. The X-ray powder diffraction spectrum of $GdRhO_3$ at 298 K. The experimental data are denoted by open circles, while the line through the circles represents the result of the Rietveld refinement. The row of vertical bars represents the Bragg peak positions for the *Pnma* space group. The lower solid line represents the difference curve between experimental and calculated spectra.

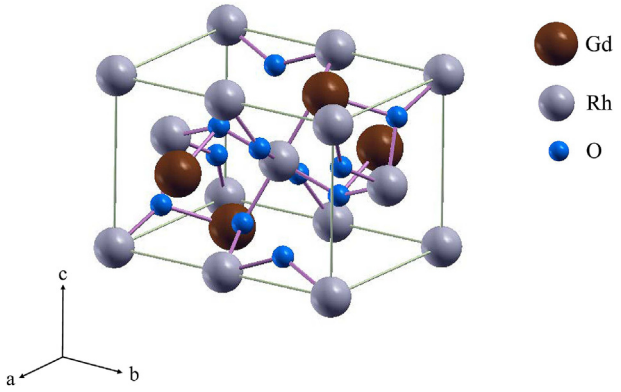

Fig. 2. The unit cell of the $GdRhO_3$ compound.

mixture of covalent and ionic bonding. Fig. 3 displays the calculated valence charge density distributions in the (001), (010), and (110) planes. Electron deficiency is colored in red, and electron excess is depicted as purple; intermediate charge densities are colored in green/blue (Fig. 3). The charge density distribution of the valence states explains the nature of the chemical bonding between the atoms in $GdRhO_3$. The presence of directional covalent bonding between the Rh and O atoms in the $[RhO_3]^{3-}$ units can be observed in Fig. 3(a) (green regions). The Gd^{3+} ions are virtually isolated from the $[RhO_3]^{3-}$ units [red regions in Fig. 3(a)], which points toward a complete electron transfer between them. This electron transfer is due to a relatively strong ionic bonding between Gd^{3+} and $[RhO_3]^{3-}$, which results from strong Coulomb interactions. In particular, the existence of such strong bonds can be explained by the large difference in electronegativity between the Gd atoms (1.20) and the O and Rh atoms (3.22 and 2.28, respectively). The complete charge transfer is clearly observed by the absence of the valence charge density [red regions in Fig. 3(a)].

The intense directional covalent bonds between the Rh and O atoms can be observed from a different perspective [green regions in Fig. 3(b)]. Due to the relatively large spatial extension of the dumbbell shape O 2*p* valence states, a considerable overlap between these states and the Rh 4*d* and 5*s* states is expected in certain directions. This leads to the sharing of the valence electrons between the O and Rh atoms [Fig. 3(b)]. The interatomic distance between the O and Rh atoms in $GdRhO_3$ is small (2.11 Å). This leads to an enhanced *s*-*p* and *p*-*d* hybridization between the Rh and O states, resulting in the directional covalent bonding between the O and Rh atoms.

These directional covalent bonds surround islands that result from the absence of electron charge density [red regions in Fig. 3(b)]. The insulating nature of the compound studied can be the result of the existence of these islands, which indicates the presence of strong ionic interactions between Gd^{3+} and $[RhO_3]^{3-}$. The connecting rods between Rh and O atoms surround regions of empty space (Fig. 2) which correspond to the red islands in Fig. 3(b). This supports the analysis above.

The insulating nature of $GdRhO_3$ can best be seen in Fig. 3(c). Although there is a large number of atoms in the (110) plane, their electrostatic interactions result in vast regions deficient in electron charge density (red and yellow regions).

Table 1
Atomic positions for the orthogonal $GdRhO_3$ (space group *Pnma*) obtained through Rietveld analysis and calculated V_{zz} (in units of 10^{21} V/m^2) and η.

Atom	Site	Point symmetry	*x*	*y*	*z*	V_{zz}	η
Gd	4*c*	.*m*.	0.4228	$\frac{1}{4}$	0.0227	1.4873	0.707
Rh	4*a*	$\bar{1}$	0.0	0.0	0.0	−0.4636	0.419
O1	4*c*	.*m*.	0.5555	$\frac{1}{4}$	0.6447	0.9525	0.671
O2	8*d*	1	0.2007	0.0619	0.3218	1.0768	0.167

3.2.2. Energy band structure

The spin-up and spin-down energy bands calculated for the energy range between −7 and 12 eV are shown in Fig. 4. The presence of an energy gap above the Fermi level is evident. It accounts for the insulating behavior of $GdRhO_3$. The origin of the energy gap is due to the strong Hubbard potential (8.2 eV) corresponding to the on-site Coulomb interaction between the highly localized Gd 4*f* electrons. For the spin-up states [Fig. 4(a)], the 4*f* bands are highly packed in a narrow energy region between −5.5 to −6.1 eV. The localization of these states is realized through their small energy dispersion in the various directions in the Brillouin zone, in contrast to that of other states. The effective mass of the electrons in these 4*f* states is relatively large due to the small energy variations along different directions in the Brillouin zone. As a result, the mobility of electrons in these states is low, and consequently these electrons do not contribute to electronic transport. In addition, since these bands are located deeply below the Fermi level, they are fully occupied and hence no transition of electronic type is expected. A relatively broader energy region between 5.7 and 9.4 eV is occupied by the Gd 5*d* states. These bands are fewer in numbers, and more spread out in energy (less localized) than the 4*f* bands.

For the spin-down state, numerous localized Gd 4*f* bands occupy the energy region between about 6.5 and 7.2 eV [Fig. 4(b)]. However, as compared to the Gd 4*f* spin-up bands, they are fewer in number. This leads to a large value of Gd magnetic moment. In addition to the Gd 4*f* bands, the Gd 5*d*, Rh 4*d*, and O 2*p* bands exist in this region and extend up to 10 eV. Since these states are located far above the Fermi level and are mainly vacant, they do not affect the physical and chemical properties of $GdRhO_3$.

In the energy range 2.6−5.5 eV, the Rh 4*d*, Rh 5*s*, and O 2*p* bands appear in both spin-up and spin-down bands (Fig. 4). The *d* bands are localized at the lower end of this region (from about 2.6 to 3.5 eV), whereas the *s* and *p* conduction bands are more delocalized and occupy a broader energy region (from about 3.5 to 5.5 eV). The large energy variations of the *s* and *p* bands along various symmetry directions in the Brillouin zone, which corresponds to a large gradient of energy in *k*-space, lead to a larger crystal momentum,

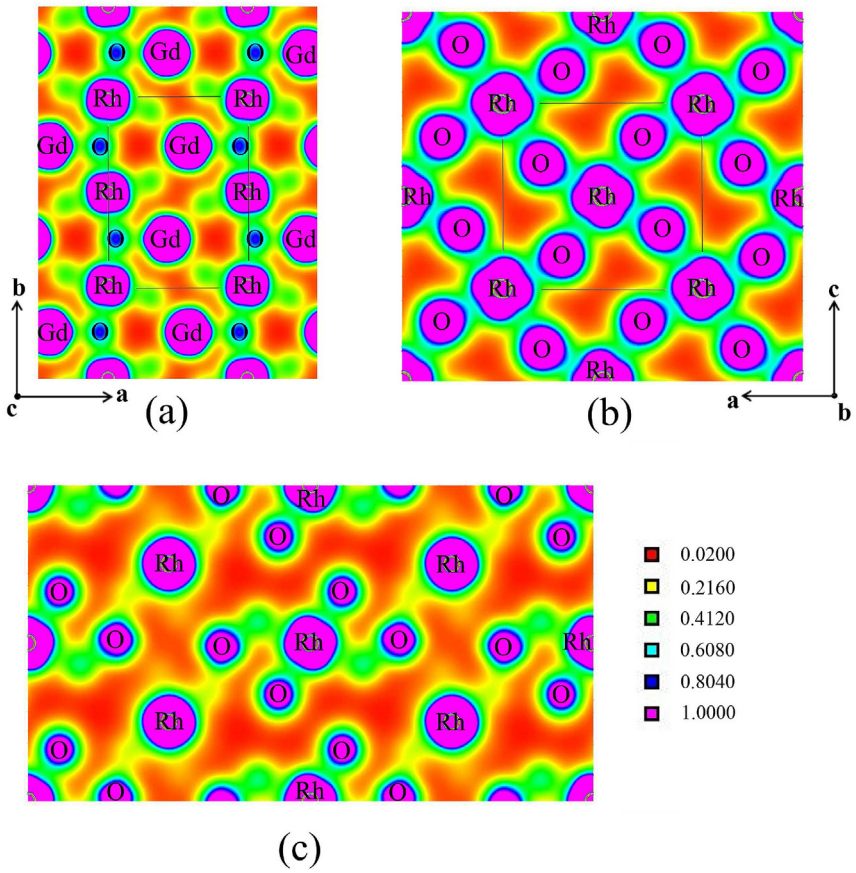

Fig. 3. Electron charge density distributions (in units of e/Å^3) in the (001) plane (a), (010) plane (b), and (110) plane (c). The unit cell boundaries are indicated in (a) and (b).

and thus results in a higher carrier mobility. This accounts for the conductive nature of these states.

Below the Fermi level, down to −5.5 eV, there is a very broad energy region of bands for both spin-up and spin-down states. These bands originate mainly from the Rh and O valence states, that is, the Rh 5*s*, Rh 4*d*, and O 2*p* states. These states, via *s*-*p* and *p*-*d* hybridization, form the aforementioned covalent bonds in the $GdRhO_3$ compound.

The numerous delocalized O 2*p* valence states occupy the region from the Fermi level and extend down to −6.0 eV. As mentioned earlier, the Coulomb interactions between electrons in the O 2*p* valence states with those in the Rh 4*d* states give rise to the formation of the covalent bonds, supporting the conclusion made earlier that was based on electron density calculations. The O 2*p* states have a relatively high energy dispersion along the various directions in the Brillouin zone, thus allowing them to share their electrons with neighboring Rh and O states. This accounts for the presence of a relatively high electron charge density in regions between these atoms.

Most of the physical and chemical properties of a material are determined by the bands in the near Fermi energy region. In the compound studied, the *d* and *s* states of the Gd and Rh atoms, and the *p* states of the O atoms, contribute to the bands in the near Fermi energy region. The numerous *f* states of Gd lie too deep in energy to have any contribution to the bands in the near Fermi energy region. The valence bands mentioned earlier and also the conduction bands merge at Γ, M, R, and X points (Fig. 4). This is explained by the high symmetry of these points which makes these states strongly degenerate. Electrons and holes near these high-symmetry points become almost immobile as their effective mass becomes increasingly large. However, the degeneracy of the valence and conduction bands is broken as one moves from one symmetry point to another. This can be observed along the Λ, Σ, Z, and Δ paths (Fig. 4). The electrons and holes along these paths still have a large, but finite effective mass which allows them to participate in a very weak form of electronic transport. The insulating nature of $GdRhO_3$ is the direct result of the characteristics of these near Fermi energy states.

The energy gap in a solid is defined as the difference in energy between the highest occupied valence band and the lowest unoccupied conduction band. In the compound studied, the smallest energy gap between the conduction and valence bands is a direct gap that occurs at the Γ point (~2.6 eV). This gap is larger than that of a typical semiconductor but smaller than the gap in most insulators. The presence of a 2.6-eV bandgap in $GdRhO_3$ (Fig. 4) could be potentially utilized in solar-cell technology. The band gap is wide enough to prevent the absorption of longer wavelengths of visible light and also of the IR radiation, thus preventing heating of the material by sunlight. On the other hand, the band gap is small enough to allow for the absorption of short wavelengths of visible light, thus generating an electrical current.

3.2.3. *Density of states*

The features of the electronic structure described above can also be observed in the total and partial density of states (DOS) of $GdRhO_3$ and its constituent atoms.

The DOS of $GdRhO_3$ (Fig. 5) contains three major features. First, two highly peaked features on both sides of the Fermi energy can be seen. They arise from the contributions made by the Gd states to the total DOS. These states are shown to be Gd 4*f* states which are

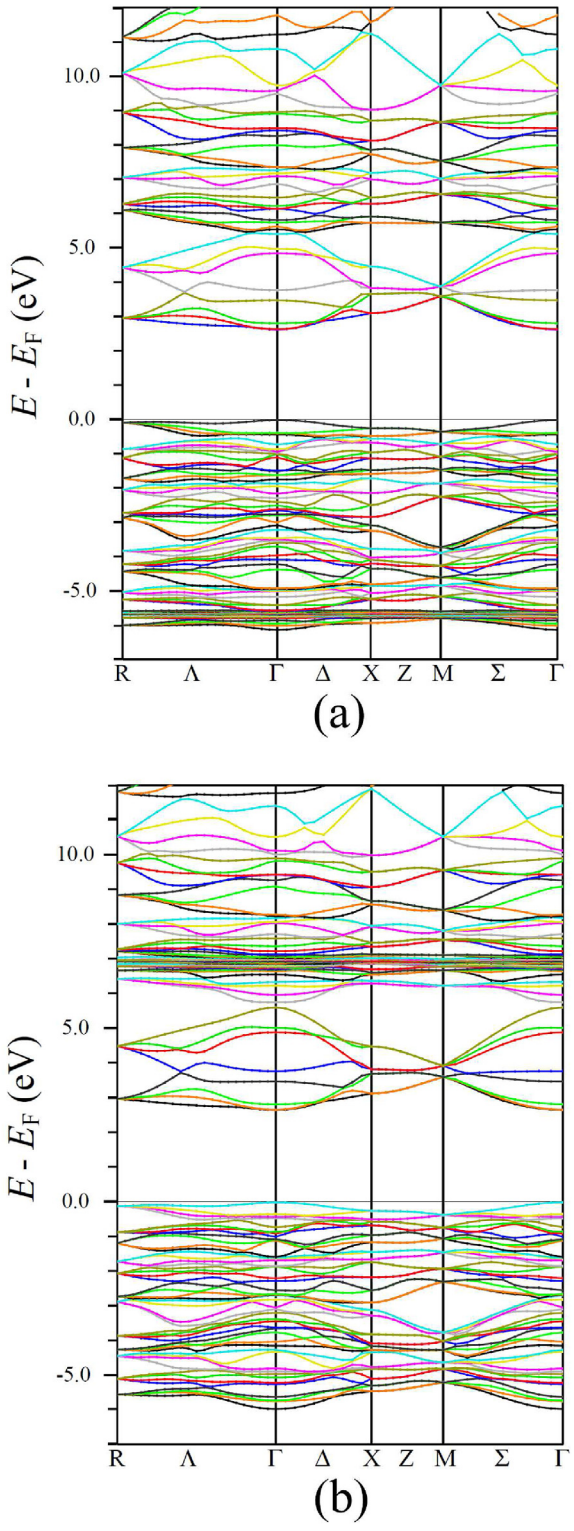

Fig. 4. Spin-up (a) and spin-down (b) band structures of $GdRhO_3$.

strongly localized in energy (Fig. 6). The strong localization of the 4*f* states is the direct consequence of using the orbital-dependent potential in the calculations. For the spin-up states, the Gd 4*f* states are localized between −5.5 and −6.1 eV, whereas for the spin-down states they are highly peaked between 6.5 and 7.2 eV. The DOS corresponding to the Gd spin-down states is smaller than that of the Gd spin-up states ((Fig. 5). Due to the large Hubbard parameter, these minority Gd 4*f* states are shifted out of the band gap. These states are empty since they lie far above the Fermi level and practically no electron would have enough energy to be excited into these states. On the other hand, the majority spin-up Gd 4*f* states can be regarded as semi-core states because they are localized in energies far below the Fermi level. This leads to the atomic-like characteristics of these states. The difference in the spin-up and spin-down Gd 4*f* DOS can explain the observed high magnetic moment of $GdRhO_3$ [5]. Since the electrons of the Gd 4*f* states are highly localized in energy and lie far from the Fermi level, they do not participate in the electronic transport in the studied compound. This is in agreement with what was discussed above based on the band structure arguments.

Second, the 2.6-eV energy gap mentioned earlier is clearly observed here (Fig. 5). This gap separates the valence states below the Fermi level from the conduction states. It explains the insulating nature of $GdRhO_3$ and thus supports the conclusions made earlier that were based on the calculated charge density distributions. The large energy separation between the Gd 4*f* states, as well as the relatively large energy gap, result from the strong Hubbard potential with an effective $U - J$ parameter of 7.52 eV.

The third feature is the presence of two regions of lower DOS (compared to the Gd DOS) that are widely spread out in energy [Fig. 5(a)]. The first region is between the Fermi level and −5.5 eV and the second region lies between 2.6 and 5.2 eV [Fig. 5(b)]. One can notice that these two energy regions are occupied by the electronic states originating from the Rh and O atoms [Fig. 5(b)] and that these states significantly overlap. Although the properties of a solid almost entirely originate from states near the Fermi level, the potential from the Gd 4*f* semi-core states affects the electrons in the 5*d* and 6*s* valence states and thus influences the distribution of these states in the Fermi energy region. One can thus state that the

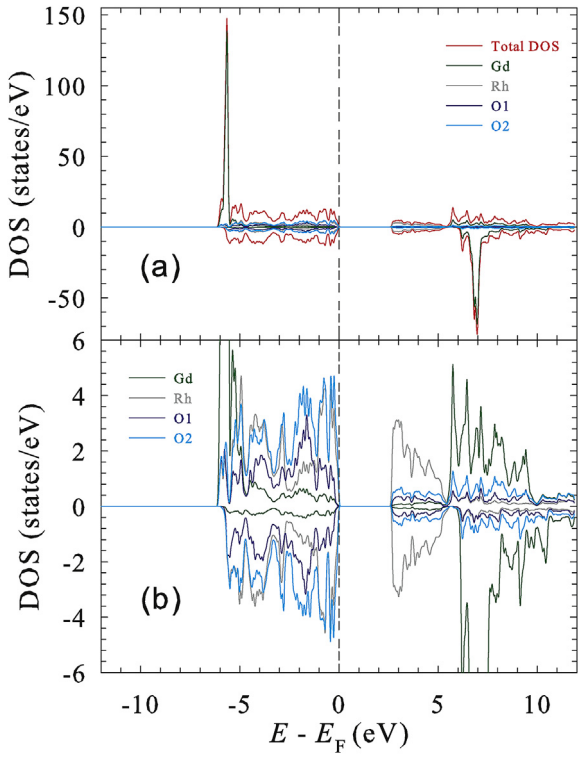

Fig. 5. (a) Spin-polarized total and atom-resolved density of states of $GdRhO_3$. (b) Idem to (a) with an enlarged vertical scale.

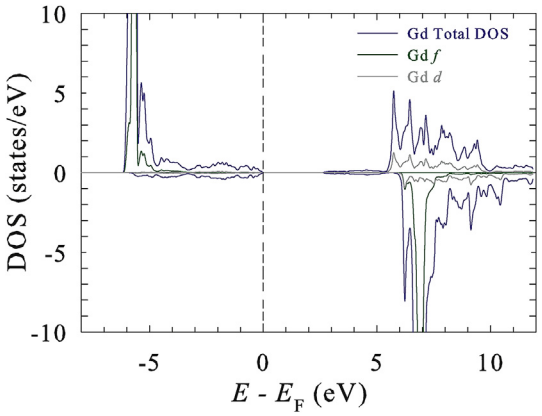

Fig. 6. Spin-polarized total and orbital-resolved density of states of Gd in $GdRhO_3$.

broad energy region occupied by the valence states is the indication of the interaction between the electrons in the 4*f* states with those in the 5*d* and 6*s* valence states. As one can see in Fig. 7, the overlap in these energy regions shows the aforementioned *p*-*d* hybridization between the Rh 4*d* and O 2*p* states. This overlap leads to the formation of directional covalent bonds between these atoms. The third feature confirms the presence of high electron density regions between the O and Rh atoms, as discussed earlier. On the other hand, the majority of the Rh and O states do not overlap with the Gd 4*f* states. This is because the Rh and O states are spread out in energy whereas the Gd states are localized. Thus, one can expect the existence of ionic bonding between the Gd and Rh/O atoms, as discussed earlier.

Upon further inspection of the atom-resolved DOS of Rh and O (Fig. 7), one notices that the spin-up and spin-down contributions are virtually identical, with the location of DOS peaks at the same energies. This results in almost zero magnetic moments of these two atoms.

3.2.4. Magnetic moments and Mössbauer parameters

The calculated total magnetic moment of $GdRhO_3$ is 7.00 μ_B. This value should be compared with the corresponding experimental value of 6.6(1) μ_B measured at 1.9 K and in an external magnetic field of 9.0 T [5].

The calculated magnetic moment of the Gd atoms is 6.9316 μ_B and the total magnetic moment of the interstitial regions is 0.10750 μ_B. The calculated magnetic moments associated with the Rh, O1, and O2 atoms are 0.00335, −0.01451, and −0.01393 μ_B, respectively. The non-zero magnetic moments associated with the Rh and O atoms are induced by the magnetic field produced by the Gd magnetic moments. This magnetic field interacts with the spins of electrons of neighboring atoms and thus modifies their energy levels depending on the spin orientation. This induces a non-zero magnetic moment on the Rh and O atoms. The Gd magnetic moments are localized and this is confirmed by the fact that the calculated Rh and O magnetic moments are very small. In other words, if the Gd 4*f* states were broadly distributed such that a significant overlap between these states and the O and Rh states existed, the magnetic moments of Rh and O would then be considerably affected, resulting in their much larger values than those predicted by calculations.

Our calculations indicate that the magnetic moment of $GdRhO_3$ almost entirely originates from the Gd atoms. This is in agreement with the calculated spin-polarized DOS (*vide supra*).

The antiferromagnetic interaction between the Gd^{3+} ions can be explained by an indirect exchange interaction via the intermediate O^{2-} ions. Due to the strong localization of the Gd 4*f* states, the super

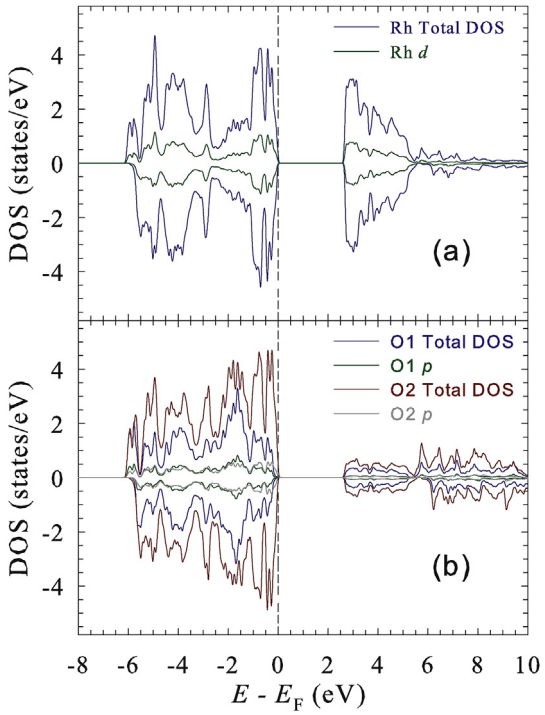

Fig. 7. Spin-polarized total and orbital-resolved density of states of Rh (a) and O (b) in $GdRhO_3$.

exchange interaction between the Gd 4*f* electrons and the O 2*p* electrons is negligible. As one can see from Fig. 5, there is not a significant overlap between the majority of the O 2*p* states and the Gd 4*f* states. However, it is the Gd 5*d* and 6*s* valence states (because of their relatively large spatial distribution) that make the interatomic exchange interaction between the Gd and O atoms through the Gd—*O*—Gd bonds possible. The distance between the Gd nearest neighbors in $GdRhO_3$ is 4.07 Å and the angle of the Gd—*O*—Gd bond is 133.6°. Due to a relatively large value of this distance, the direct exchange interaction between the Gd spins is not possible. Therefore, the nature of the antiferromagnetic coupling must be of the indirect type. Because of the overlap between the O 2*p* states and the Gd valence states, there is always a nonzero probability of electron spin interaction between the O 2*p* states and the Gd valence states and hence an indirect exchange interaction via the Gd—*O*—Gd path is expected.

The calculated V_{zz} and η at the Gd, Rh, O1, and O2 sites are given in Table 1. The calculated H_{hf} at the Gd site is 283.3 kOe. The calculated V_{zz}, η, and H_{hf} at the Gd site will be compared with the corresponding experimental values below.

3.3. Magnetic measurements

Fig. 8(a) shows the temperature dependence of the magnetic susceptibility χ of $GdRhO_3$ measured in an applied magnetic field of 1.0 kOe. The peak at $T_N = 2.13(5)$ K in the $\chi(T)$ data [inset in Fig. 8(a)] is indicative of antiferromagnetic ordering occurring at this temperature.

The $\chi(T)$ data above 20 K [Fig. 8(a)] could be fitted to a modified Curie-Weiss law

$$\chi = \chi_0 + \frac{C}{T - \Theta_p}, \tag{2}$$

where χ_0 is the temperature-independent magnetic susceptibility

that includes contributions from Pauli and Van Vleck paramagnetism as well as from core and Landau diamagnetism, C is the Curie constant, and Θ_p is the paramagnetic Curie temperature. The Curie constant can be expressed as $C = \frac{N\mu_{eff}^2}{3k_B}$, where N is the number of Gd atoms per formula unit, μ_{eff} is the effective magnetic moment, and k_B is the Boltzmann constant. The inverse magnetic susceptibility corrected for the contribution χ_0 as $(\chi - \chi_0)^{-1}$ versus temperature is shown in Fig. 8(b); the data clearly satisfy the modified Curie-Weiss law. The values of χ_0, C, and Θ_p obtained from the fit are, respectively, $5.43(1.82) \times 10^{-8}$ cm^3/g, $25.92(1) \times 10^{-3}$ cm^3 K/g, and $-3.37(1)$ K. This value of C corresponds to $\mu_{eff} = 7.99(1)\ \mu_B$ per Gd atom.

For a free Gd^{3+} ion (electronic configuration $^8S_{7/2}$), the theoretical value of $\mu_{eff}^{th} = g\mu_B\sqrt{J(J+1)}$ is 7.94 μ_B [15]. From the fact that the experimental value $\mu_{eff} = 7.99(1)\ \mu_B$ is close to the theoretical value of 7.94 μ_B it is concluded that the magnetic moment is localized on the Gd^{3+} ions and that, as expected, Rh atoms carry no magnetic moment. The negative value of Θ_p indicates that the interaction between the Gd^{3+} spins is predominantly antiferromagnetic.

3.4. Mössbauer spectroscopy

The ^{155}Gd Mössbauer spectrum of $GdRhO_3$ measured at 5.6 K, i.e., in the paramagnetic region above T_N, is shown in Fig. 9. The crystallographic site at which the Gd^{3+} ions are located has the point symmetry .m. (Table 1), which implies a non-zero EFG at the Gd^{3+} site, and hence a non-zero electric quadrupole hyperfine interaction. The Mössbauer spectrum in Fig. 9 indeed shows the presence of a substantial electric quadrupole hyperfine interaction and the absence of the magnetic dipole hyperfine interaction. The absence of the magnetic dipole hyperfine interaction in the Mössbauer spectrum in Fig. 9 proves that at 5.6 K the Gd magnetic moments are not magnetically ordered. For ^{155}Gd nuclei, the quadrupole moment of the excited nuclear state $Q_{ex} = 0.12$ b [8] is significantly smaller than that of the ground nuclear state $Q_g = 1.30$ b [16]. Consequently, the quadrupole splitting of the excited nuclear state, which is sensitive to the sign of V_{zz} and the magnitude of η, is smaller than the natural linewidth $\Gamma_{nat} = 0.250$ mm/s. As a result, only the absolute value of the effective quadrupole splitting parameter $\Delta_g^{eff} = eQ_g\left|V_{zz}\right|\sqrt{1+\eta^2/3}$ can be derived from a Mössbauer spectrum of a sample in the paramagnetic state and the spectrum, which consists of six lines, has the appearance of a doublet [17].

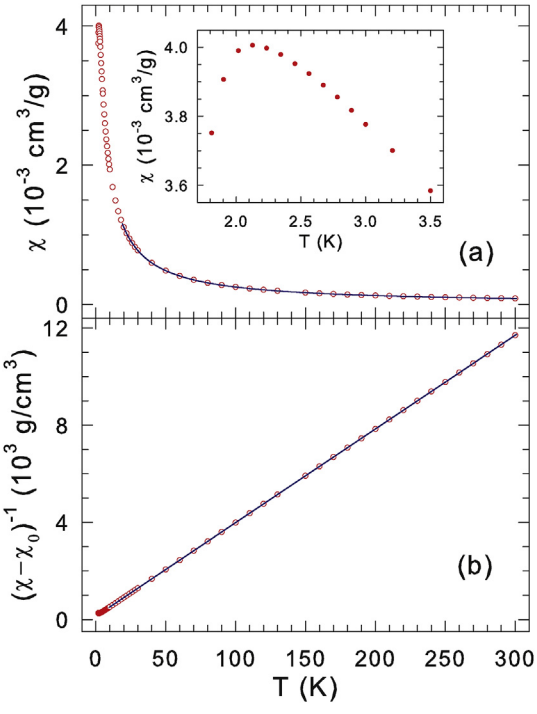

Fig. 8. (a) Temperature dependence of the magnetic susceptibility of $GdRhO_3$, measured in an external magnetic field of 1.0 kOe. The solid line is the fit to Eq. (2) in the temperature range 20–300 K, as explained in the text. The inset shows the magnetic susceptibility data in the low-temperature range. (b) Temperature dependence of the inverse magnetic susceptibility corrected for the contribution χ_0, $(\chi - \chi_0)^{-1}$ of $GdRhO_3$. The solid line is the fit to Eq. (2).

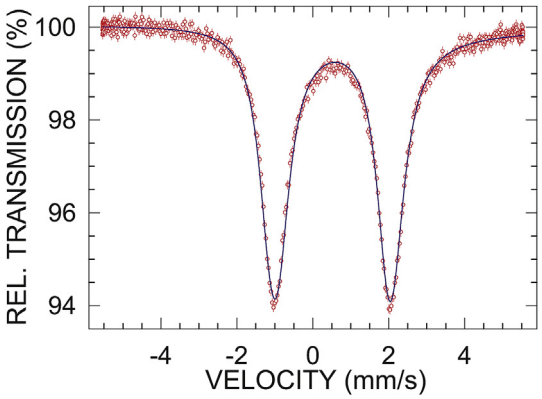

Fig. 9. ^{155}Gd Mössbauer spectrum of $GdRhO_3$ at 5.6 K fitted (solid line) with an electric quadrupole hyperfine interaction, as described in the text. The zero-velocity origin is relative to the source.

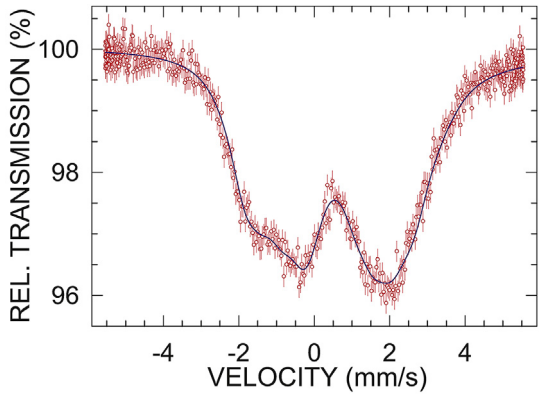

Fig. 10. ^{155}Gd Mössbauer spectrum of $GdRhO_3$ at 1.6 K fitted (solid line) with a combined magnetic dipole and electric quadrupole hyperfine interactions, as described in the text. The zero-velocity origin is relative to the source.

The fit of the Mössbauer spectrum in Fig. 9 yields the following parameters: the isomer shift [relative to the ^{155}Eu($SmPd_3$) source] $\delta = 0.505(2)$ mm/s, $\Delta_g^{eff} = 6.402(8)$ mm/s, $f_a = 17.1(1)\%$, and $\Gamma_a = 0.294(6)$ mm/s. The value of δ confirms the trivalent state of Gd in $GdRhO_3$ [17].

For the lattice vibrations treated in terms of the Debye approximation, the absorber Debye-Waller factor f_a is expressed [7] by the Debye temperature, Θ_D, as

$$f_a(T) = \exp\left\{ -\frac{3}{4}\frac{E_\gamma^2}{Mc^2 k_B \Theta_D}\left[1 + 4\left(\frac{T}{\Theta_D}\right)^2 \int_0^{\Theta_D/T} \frac{x dx}{e^x - 1}\right]\right\}, \quad (3)$$

where E_γ is the energy of the Mössbauer transition, M is the mass of the Mössbauer nucleus, and c is the speed of light. The value of $f_a = 17.1(1)\%$ derived from the fit of the Mössbauer spectrum in Fig. 9 gives via Eq. (3) $\Theta_D = 256(1)$ K. The value of Θ_D found here is close to the value of 271 K determined from the specific heat data for the $LuRhO_3$ orthorhodite [3].

Fig. 10 shows the ^{155}Gd Mössbauer spectrum of $GdRhO_3$ at 1.6 K, i.e., below T_N. This spectrum clearly exhibits the presence of a combined magnetic dipole and electric quadrupole hyperfine interactions. The fit of such a spectrum, which consists of 24 lines, allows both the sign of V_{zz} and the value of η to be determined. The presence of the magnetic dipole hyperfine interaction in the Mössbauer spectrum in Fig. 10 proves that the Gd magnetic moments are magnetically ordered at 1.6 K. The following parameters were derived from the fit (because of the strong correlation between the values of η and the angle ϕ, the latter had to be constrained to the value of 0.0°) of the Mössbauer spectrum in Fig. 10: $\delta = 0.505(1)$ mm/s, $H_{hf} = 219.7(3.4)$ kOe, the quadrupole splitting constant $eQ_gV_{zz} = 5.480(24)$ mm/s [$V_{zz} = 1.216(5) \times 10^{22}$ V/m^2], $\eta = 0.98(5)$, the angle $\theta = 35.2(2.1)^\circ$, and $f_a = 18.2(9)\%$. A substantial value of H_{hf} indicates a considerable magnetic moment of Gd atoms.

We note here that the experimental value of H_{hf} is smaller than the calculated value of 283.3 kOe. However, the agreement between the experimental values of V_{zz} and η and the calculated ones (1.4873×10^{22} V/m^2 and 0.707) is much more satisfactory.

The point symmetry *.m.* (Table 1) of the 4*c* site occupied by the Gd atoms stipulates the existence of a mirror plane perpendicular to the crystallographic *b*-axis. Consequently, one of the principal axes of the EFG tensor has to be parallel to the crystallographic *b*-axis and the two other EFG principal axes lie in the *ac*-plane [18]. If V_{zz} is parallel to the *b*-axis than the fitted parameter $\theta = 35.2(2.1)^\circ$ and the assumed $\phi = 0.0^\circ$ imply that the hyperfine magnetic field at the Gd site, and hence the Gd magnetic moment, is $35.2(2.1)^\circ$ off the *b*-axis in the *bc*-plane.

4. Summary

We report the results of X-ray diffraction, magnetic, and ^{155}Gd Mössbauer spectroscopy study, complemented by the *ab-initio* electronic structure and the hyperfine interaction parameters calculations, of the $GdRhO_3$ orthorhodite. It is shown that this compound crystallizes in the orthorhombic space group *Pnma* with the lattice parameters $a = 5.7450(1)$ Å, $b = 7.6647(1)$ Å, and $c = 5.2905(1)$ Å. Evidence for the presence of directional covalent bonding between the Rh and O atoms and of ionic bonding between the Gd and Rh/O atoms is provided. $GdRhO_3$ develops long-range antiferromagnetic order with the Néel temperature $T_N = 2.13(5)$ K. The temperature dependence of the magnetic susceptibility above T_N follows the modified Curie-Weiss law, with the effective magnetic moment of 7.99(1) μ_B per Gd atom and the paramagnetic Curie temperature of −3.37(1) K. The Debye temperature of $GdRhO_3$ is found to be 256(1) K. The calculated hyperfine-interaction parameters and the Gd magnetic moment are in good agreement with the experimental values.

Acknowledgements

This work was supported by the Natural Sciences and Engineering Research Council of Canada.

References

[1] a) A. Wold, B. Post, E. Banks, J. Am Chem. Soc. 79 (1957) 6365;
b) A. Wold, R.J. Arnot, W.J. Croft, Inorg. Chem. 2 (1963) 972;
c) R.D. Shannon, Acta Cryst. B 26 (1970) 447;
d) I.S. Shaplygin, I.I. Prosychev, V.B. Lazarev, Russian J. Inorg. Chem. 31 (1986) 1649;
e) V.N. Skrobot, V.L. Ugolkov, S.K. Kuchaeva, D.P. Romanov, R.G. Grebenshchikov, V.V. Gusarov, Russian J. Inorg. Chem. 51 (2006) 1116;
f) R.B. Macquart, M.D. Smith, H.-C. zur Loye, Cryst. Growth Design 6 (2006) 1361.
[2] H.S. Jarrett, A.W. Sleight, H.H. Kung, J.L. Gillson, J. Appl. Phys. 51 (1980) 3916.
[3] W. Yi, Q. Liang, Y. Matsushita, M. Tanaka, X. Hu, A.A. Belik, J. Solid State Chem. 200 (2013) 271.
[4] T. Taniguchi, W. Iizuka, Y. Nagata, T. Uchida, H. Samata, J. Alloys Compd. 350 (2003) 24.
[5] T. Ohnishi, T. Taniguchi, A. Ikoshi, S. Mizusaki, Y. Nagata, S.H. Lai, M.D. Lan, Y. Noro, T.C. Ozawa, K. Kindo, A. Matsuo, S. Takayanagi, J. Alloys Compd. 506 (2010) 27.
[6] B.F. Otterloo, Z.M. Stadnik, A.E.M. Swolfs, Rev. Sci. Instrum. 54 (1983) 1575.
[7] a) N.N. Greenwood, T.C. Gibb, Mössbauer Spectroscopy, Chapman and Hall, London, 1971;
b) P. Gütlich, E. Bill, A. Trautwein, Mössbauer Spectroscopy and Transition Metal Chemistry, Springer, Berlin, 2011.
[8] H. Armon, E.R. Bauminger, S. Ofer, Phys. Lett. B 43 (1973) 380.
[9] Z. M. Stadnik and J. Żukrowski (unpublished).
[10] a) S. Margulies, J.R. Ehrman, Nucl. Instrum. Methods 12 131 (1961);
b) G.K. Shenoy, J.M. Friedt, H. Maletta, S.L. Ruby, in: I.J. Gruverman, C.W. Seidel, D.K. Dieterly (Eds.), Mössbauer Effect Methodology 10, Plenum, New York, 1974, p. 277.
[11] P. Blaha, K. Schwartz, G. Madsen, D. Kvasnicka, J. Luitz, WIEN2k, an Augmented Plane Wave Plus Local Orbitals Program for Calculating Crystal Properties, Karlheinz Schwarz, Technical Universität Wien, Austria, 1999.
[12] J.P. Perdew, S. Burke, M. Ernzerhof, Phys. Rev. Lett. 77 (1996) 3865.
[13] M. Raekers, K. Kepper, S. Bratkowski, M. Prinz, A.V. Postnikov, K. Potzger, S. Zhou, A. Arulraj, N. Stüßer, R. Uecker, W.L. Yang, M. Neumann, Phys. Rev. B 79 (2009) 125114.
[14] R.A. Young, The Rietveld Method, Oxford University Press, Oxford, 1993.
[15] N.W. Ashcroft, N.D. Mermin, Solid State Physics, Saunders, Philadelphia, 1976.
[16] Y. Tanaka, D.B. Laubacher, R.M. Steffen, E.B. Shera, H.D. Wohlfahrt, M.V. Hoehn, Phys. Lett. B 108 (1982) 8.
[17] G. Czjzek, in: G.J. Long, F. Grandjean (Eds.), Mössbauer Spectroscopy Applied to Magnetism and Materials Science vol. 1, Plenum, New York, 1993, p. 373.
[18] K. Tomala, R. Kmieć, R. Kruk, G. Czjzek, J. Magn. Magn. Mater 222 (2000) 285.